IEEE Photonics Journal
An IEEE Photonics Society Publication

Optimized Dipole-Surface Plasmon Waveguide Coupling for Enhancement of SLD Performance

Volume 2, Number 5, October 2010

M. Ranjbaran, Student Member, IEEE
X. Li, Senior Member, IEEE

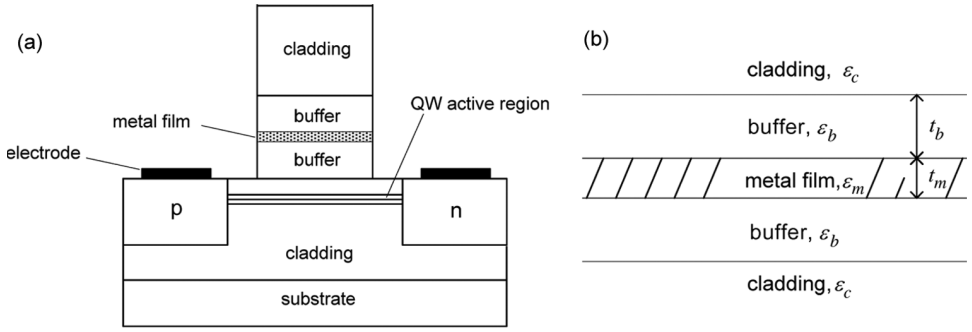

DOI: 10.1109/JPHOT.2010.2072954
1943-0655/$26.00 ©2010 IEEE

Optimized Dipole-Surface Plasmon Waveguide Coupling for Enhancement of SLD Performance

M. Ranjbaran, *Student Member, IEEE*, and X. Li, *Senior Member, IEEE*

Department of Electrical and Computer Engineering, McMaster University, Hamilton, ON L8S 4K1, Canada

DOI: 10.1109/JPHOT.2010.2072954
1943-0655/$26.00 ©2010 IEEE

Manuscript received June 20, 2010; revised August 24, 2010; accepted August 26, 2010. Date of publication September 2, 2010; date of current version September 24, 2010. Corresponding author: M. Ranjbaran (e-mail: ranjbam@mcmaster.ca).

Abstract: A five-layer surface plasmon waveguide (SPWG) is proposed to be used in a superluminescent diode. It is shown that the generated light by the proposed device has higher power and broader spectrum compared with a conventional device in which a dielectric waveguide has been used. The effect of SPWG parameters on loss and spontaneous emission coupling factor is addressed, and design guidelines have been given for two cases where emphasis is on high output power or high power-spectral width product.

Index Terms: Superluminescent diodes, quantum well devices.

1. Introduction

Plasmonics is an active field of research in optics which promises the advent of nanoscale optoelectronic systems by subwavelength confinement of electromagnetic fields. Observation of some extraordinary phenomena resulting from the electromagnetic field enhancement can lead to novel devices and applications [1]. Here, a key role is played by plasmons or unbound electrons at the surface of or localized in conducting nanostructures. Many areas of application, such as waveguiding and passive waveguide devices [1], [2], sensing and detection [3], near-field microscopy [4], and nanoscale manipulation [5], have already opened up.

The application of plasmonics in light-generating devices such as quantum-cascade lasers (QCLs) and light-emitting diodes (LEDs) have already been well established [6], [7]. QCL emission now spans the mid to far infrared part of the electromagnetic spectrum, where metal loss is relatively small. In surface-emitting LEDs metal, which is usually in the form of patterned films (gratings), is used to efficiently extract light out of the cavity. Here, we propose the use of surface plasmon waveguide (SPWG) in superluminescent diodes (SLDs). Similar to the laser diode (LD), the SLD benefits from the optical gain of an active region to achieve a high output power but avoids lasing in the cavity to get a wide emission linewidth (the word linewidth is used hereafter to refer to the spectral width). As lasing in the cavity is the main source of the optical power coming out of a LD, an important challenge in the design of the SLD is dealing with the tradeoff of having both high power and broad linewidth (or equivalently having high power-linewidth product). A number of techniques have been used either to broaden the material gain spectrum [8], [9] or to make facet reflection and cavity length as small as possible in order to broaden the output power spectrum [10]–[12]. Replacing the conventional dielectric waveguide with the SPWG, as shown by this work,

is another way to push the power-linewidth product further high and can be applied in combination with other methods to achieve maximum possible power-linewidth product for SLDs.

A 1-D analytical formulation of the output power and its linewidth presented by Park and Li [13] shows the nature of power-linewidth trade off and suggests a possible way to improve it. According to them, the peak output power is given by

$$P_p = \frac{2\beta n_{sp} hc^2}{\lambda_p^3} \exp\{-\alpha L + G(N)\} \tag{1}$$

and the output spectrum has a Gaussian shape with a full-width at half-maximum (FWHM) of

$$\Delta\lambda_{FWHM} \propto \frac{\lambda_w(N)}{\sqrt{G(N)}} \tag{2}$$

The parameters in (1) are as follows: h is the Planck constant, c is the speed of light in a vacuum, β is the portion of the spontaneously emitted light coupled to the guided wave (or simply the spontaneous emission coupling factor), n_{sp} is the population inversion factor, λ_p is the peak gain wavelength, λ_w is the half width of the parabolic material gain profile (full width defined by zero crossing points), α is the modal loss, L is the device length, N is the carrier density, and G is the total device gain given by

$$G(N) = L\Gamma g_0(N) \tag{3}$$

in which Γ is the confinement factor, and g_0 is the peak material gain.

$G(N)$ appears in the denominator of (3) so that an increase of the output power by increasing the device length is followed by a reduction in the spectral width. When the injection current is increased, however, two counter acting effects take place; the total device gain $G(N)$ increases, but at the same time, the gain profile becomes broader due to the so-called band-filling effect. The first effect, as seen from (2), tends to reduce the spectral width $\Delta\lambda_{FWHM}$, while the second one acts in the opposite way. As a result, $\Delta\lambda_{FWHM}$ may increase or decrease. Therefore, for an optimized material gain profile, if the spectral width sets an upper limit on the total device gain, increasing β, as suggested by (1), seems to be the only way to achieve a higher output power without the cost of spectral width reduction.

The spontaneous emission coupling factor is typically on the order of $10^{-5} \sim 10^{-4}$ for LDs and $10^{-3} \sim 10^{-2}$ for SLDs and semiconductor optical amplifiers (SOA) with the conventional dielectric waveguides [14]. For SPWGs, however, β is expected to be higher [15]. In an earlier work, the authors proposed the use of SPWG in SLD instead of the conventional dielectric waveguides [15]. In this paper, first, a five-layer SPWG structure is introduced, and its important functional parameters are addressed. Next, dipole coupling to the new SPWG is considered, and the effect of various parameters on the spontaneous emission coupling factor is discussed. Finally, simulation results are presented which compare the performance of the proposed and the conventional devices in terms of the output power, emission linewidth, and the product of the two, which is a commonly used figure of merit for SLDs.

2. Proposed Structure

The schematic of the proposed device structure is shown in Fig. 1(a). The SPWG is a five-layer symmetric structure consisting of cladding/buffer/metal/buffer/cladding (CBMBC) layers, respectively, as shown in Fig. 1(b). Buffer layers have a higher refractive index than the claddings do. Similar to the three-layer cladding/metal/cladding (CMC) structure [16], the CBMBC structure

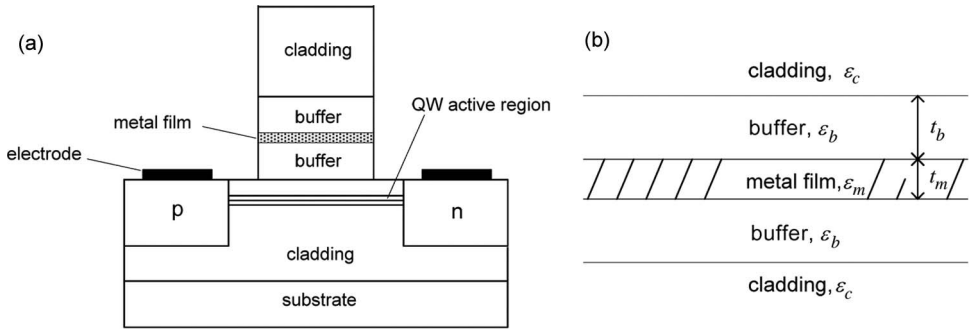

Fig. 1. (a) Schematic cross section of the proposed SLD structure with SPWG with lateral carrier injection. (b) Schematic structure of the five-layer SPWG.

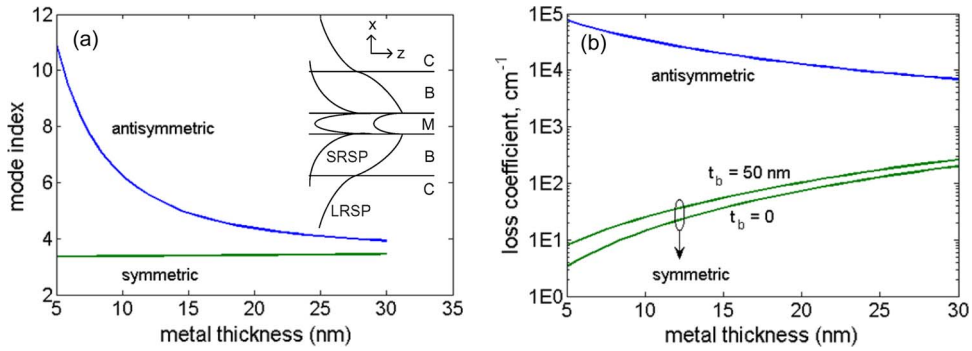

Fig. 2. (a) Mode index and (b) loss coefficient of the five-layer CBMBC structure versus metal film thickness for symmetric (LRSP) and antisymmetric (SRSP) modes. Inset: $|H_y|$ of LRSP and SRSP modes.

supports two symmetric and antisymmetric bound surface plasmon modes concentrated at the surfaces of the metal film and extending into the claddings. The quantum well (QW) active region lies on one side of the film in the cladding, and carriers are injected laterally into the active region [15], [17].

3. Propagation Constants and Waveguide Loss

At the interested wavelength region of near infrared, the propagation constant is complex $(\gamma = \beta_r - i\beta_i)$ primarily due to the loss of metal, which is usually silver or gold. Fig. 2 shows the mode index $(\beta_r/\omega\sqrt{\mu_0\varepsilon_0})$ and loss coefficient $(2\beta_i)$ of the proposed five-layer SPWG versus thickness of the metal layer for the symmetric and antisymmetric modes. The parameters used are $\lambda = 1.55$ μm, $\varepsilon_c = 11.2$, $\varepsilon_b = 12.25$, $\varepsilon_m = -116.38 - 11.1i$ (silver at the specified wavelength [18]), and $t_b = 50$ nm. For comparison, the loss coefficient of a CMC structure (i.e., $t_b = 0$) has also been drawn. Compared with the symmetric mode, the antisymmetric mode has a huge loss, which makes it inapplicable for an active device; hence, we have the names long-range (LRSP) and short-range surface plasmon (SRSP) for the two modes. Note the logarithmic scale of Fig. 2(b) indicating rapid increase of loss with increasing film thickness. In terms of the output power, therefore, the metal film should be as thin as possible. The inset of Fig. 2 shows the schematic profile of the $|H_y|$ component of LRSP and SRSP modes. While the schematic profiles are not to be scaled, one should note that the SRSP mode is mainly confined inside the metal film and decays much faster outside it than does the LRSP mode. Fig. 3 shows the variation of loss coefficient for the symmetric mode with buffer thickness for different values of buffer refractive index. An increase in the dielectric constant of the buffer layer increases the loss. Also, when the refractive index of buffers is smaller than that of the claddings, loss decreases with increasing buffer thickness until the symmetric mode is cut off. The effect of the buffer layer on the spontaneous emission coupling factor will be considered in the

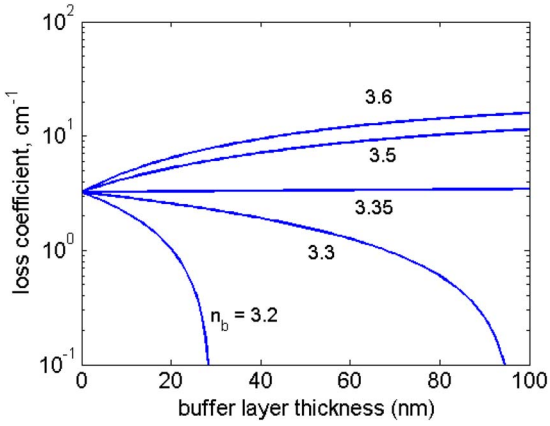

Fig. 3. Loss coefficient of symmetric mode of the structure of Fig. 1(a) as a function of buffer thickness for various values of buffer refractive index. Other parameters are the same as those for Fig. 2.

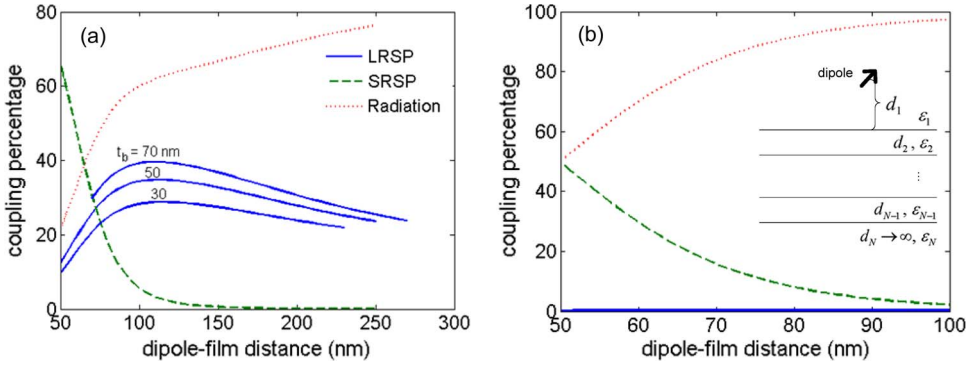

Fig. 4. Dipole coupling to LRSP, SRSP, and radiation modes of the structure of Fig. 1 with a 10-nm thick QW separated 115 nm from the metallic film. Metal film thickness is 5 nm. Other parameters are the same as those used for Fig. 2. (a) Perpendicular dipole. (b) Parallel dipole. Inset: Planar structure below a dipole.

next section. Figs. 2 and 3 are obtained by finding the dispersion relations of the structure using the transfer matrix method [19] and solving them with the argument principle method [20].

4. Spontaneous Emission Coupling Factor

Electron-hole pairs injected into the active region of the proposed device excite symmetric/antisymmetric guided as well as radiation modes of the SPWG. We model an electron-hole pair as a harmonic oscillator (dipole) driven by the reflection of its own field due to the presence of an optical structure [21]. A radiating electric dipole has a lifetime (τ) that depends on the properties of the structure in which it is embedded. If the structure supports optical modes, the decay rate $(b = 1/\tau)$ is higher than when the dipole is embedded in free space. For a dipole embedded in a nonmagnetic medium with refractive index n_1 and wavenumber k_1, the normalized decay rate is [21]

$$\hat{b}(= b/b_0) = 1 + \frac{3n_1^2}{2\mu_0 k_1^3}\,\mathrm{Im}(E_0) \tag{4}$$

where E_0 is the complex amplitude of the reflected electric field of the emitting dipole at the dipole position, and b_0 is the free space decay rate.

Consider a planar structure under an electric dipole as depicted in the inset of Fig. 4. The electromagnetic field radiated by the dipole can be decomposed into plane waves of different wave

vectors. Those plane waves with the parallel component of their wave vectors smaller than k_1 are called radiative components as they cannot propagate as a bounded mode and radiate away from the structure. The rest cannot propagate laterally in the dipole medium (evanescent waves in the vertical direction) and are called nonradiative components. All guided modes of the structure, including any SP modes are, therefore, in the nonradiative part of the dipole emission. Accordingly, the normalized decay rate is decomposed into radiative and nonradiative parts

$$\hat{b} = \hat{b}_r + \hat{b}_{nr}. \tag{5}$$

These decay rates are obtained by solving Maxwell's equations using, for example, the dyadic Green's function method. Adopting the notation of [21], the results for dipoles with perpendicular $(\perp)$ and parallel $(\|)$ orientations (relative to the planar structure) are

$$\hat{b}_r^{\perp} = 1 + \frac{3}{2}\mathrm{Im}\left\{\int_0^1 f_1' e^{-2l_1\hat{d}_1}\frac{u^3 du}{l_1}\right\} \tag{6a}$$

$$\hat{b}_{nr}^{\perp} = \frac{3}{2}\mathrm{Im}\left\{\int_1^{\infty} f_1' e^{-2l_1\hat{d}_1}\frac{u^3 du}{l_1}\right\} \tag{6b}$$

$$\hat{b}_r^{\|} = 1 + \frac{3}{4}\mathrm{Im}\left\{\int_0^1 \left[(u^2-1)f_1' + c_1'\right] e^{-2l_1\hat{d}_1}\frac{u du}{l_1}\right\} \tag{6c}$$

$$\hat{b}_{nr}^{\|} = \frac{3}{4}\mathrm{Im}\left\{\int_1^{\infty} \left[(u^2-1)f_1' + c_1'\right] e^{-2l_1\hat{d}_1}\frac{u du}{l_1}\right\}. \tag{6d}$$

Coefficients f_1' and c_1' are calculated from

$$f_1' = -\frac{R_{12}^{\|} + \mathbb{S}_2}{1 + R_{12}^{\|}\mathbb{S}_2} \tag{7a}$$

$$c_1' = \frac{R_{12}^{\perp} + \mathbb{R}_2}{1 + R_{12}^{\perp}\mathbb{R}_2} \tag{7b}$$

where $\mathbb{S}_2$ and $\mathbb{R}_2$ are given by recursive relations

$$\mathbb{S}_n = \frac{R_{n,n+1}^{\|} + \mathbb{S}_{n+1}}{1 + R_{n,n+1}^{\|}\mathbb{S}_{n+1}} e^{-2l_n\hat{d}_n} \tag{8a}$$

$$\mathbb{R}_n = \frac{R_{n,n+1}^{\perp} + \mathbb{R}_{n+1}}{1 + R_{n,n+1}^{\perp}\mathbb{R}_{n+1}} e^{-2l_n\hat{d}_n} \tag{8b}$$

with $\mathbb{S}_N = \mathbb{R}_N = 0$. $R_{n,n+1}^{\perp}$ and $R_{n,n+1}^{\|}$ are the Fresnel reflection coefficients of a ray with perpendicular and parallel polarizations, respectively, incident from medium n to $n+1$, and are given as

$$R_{n,n+1}^{\perp} = \frac{l_n - l_{n+1}}{l_n + l_{n+1}} \tag{9a}$$

$$R_{n,n+1}^{\|} = \frac{\varepsilon_n l_{n+1} - \varepsilon_{n+1} l_n}{\varepsilon_n l_{n+1} + \varepsilon_{n+1} l_n} \tag{9b}$$

Other parameters are $\hat{d}_j = k_1 d_j$, $k_1 = \varepsilon_1^{1/2}\omega/c$, and $l_j = -i\left(\varepsilon_j/\varepsilon_1 - u^2\right)^{1/2}$ for $j = 1, 2, \ldots, N$.

The five-layer structure of Fig. 1(b) has two guided SP modes, meaning that the integrands in (6b) and (6d) pass through two peaks corresponding to two complex poles when u equals the

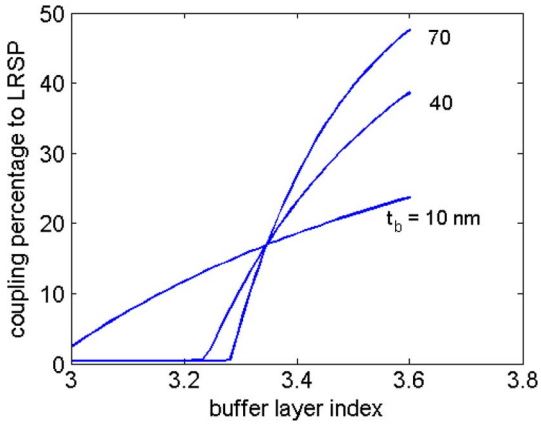

Fig. 5. Maximum dipole coupling to LRSP for a five-layer SPWG as a function of buffer refractive index for different values of buffer thicknesses. Dipole distance from the metal film is 115 nm. Other parameters are the same as those used for Fig. 2.

propagation constants of the two modes. The first (left) peak belongs to the symmetric mode and is sharper than the other one. Different spontaneous emission coupling factors are now defined by

$$\beta = \frac{\hat{b}_p}{\hat{b}} \tag{10}$$

where $\hat{b}_p$ is the pole contribution of the SP modes to (6b) and (6d) or contribution of radiation modes as given by (6a) and (6c). Fig. 4 shows the coupling factors for symmetric, antisymmetric, and radiation modes of the proposed SPWG as functions of dipole distance from the metallic film for perpendicular and parallel dipoles. The decay rate $\hat{b}_p$ for a certain SP mode depends on (i) overlap of the dipole filed and field pattern of the SP mode and (ii) density of the SP mode determined from its dispersion curve [22]. Since, for the thin film structure, the density of asymmetric mode is always larger than that of the symmetric mode (see the dispersion curves in e.g., [22]), at small dipole-film distances where both LRSP/SRSP modes have comparable overlap with the dipole field, coupling to SRSP mode dominates. As dipole-film distance starts to increase, the SRSP mode decays rapidly, resulting in a rapid decrease in the dipole-SP mode field overlap and, consequently, a rapid decrease in the coupling factor of SRSP relative to the coupling factor of LRSP. Finally, when the dipole-film distance further increases, the dipole-LRSP mode field overlap falls, and coupling to LRSP mode declines. In this regime, coupling to radiation modes prevails.

As is apparent from Fig. 4(b), parallel dipole coupling to symmetric mode is very weak. Therefore, it is desirable that the QW active region generates perpendicular rather than parallel dipoles. Fig. 4(a) also shows the coupling of perpendicular dipole to the symmetric mode for two other buffer thicknesses. For buffer layers with high enough refractive indices, increasing buffer thickness causes the coupling factor to increase but increases waveguide loss as well. This indicates a tradeoff between loss and coupling factor. The dipole-film distance corresponding to the maximum coupling to LRSP is not as sensitive to the buffer thickness and refractive index as it is to other structural parameters such as metal film thickness. In Fig. 4(a), this optimal distance is $\sim$115 nm.

Fig. 5 shows perpendicular dipole coupling factor as a function of buffer refractive index for different values of buffer thickness. All curves, as expected, intersect at $n = n_c$, where there exists essentially no buffer layer.

5. Facet Reflectivity

The output of SLD is the broadband amplified spontaneous emission (ASE). Any round trip reflection from the facets reduces the emission linewidth and creates ripples in the output due to formation of cavity modes. It is, therefore, crucial to eliminate facet reflection. The outcoupling of SP modes from a

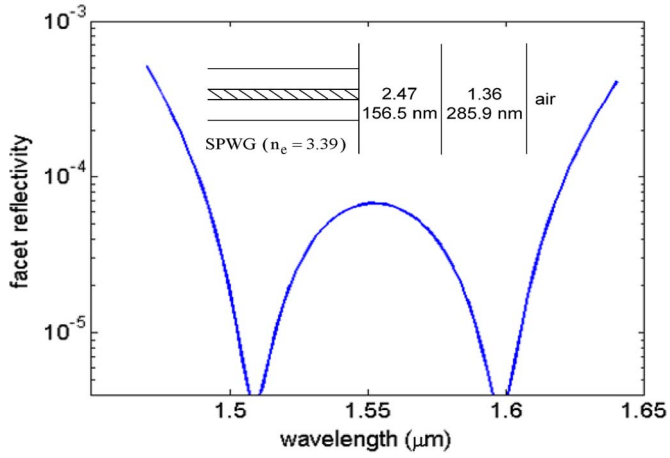

Fig. 6. Facet reflectivity with a two-layer AR coating. Inset: Schematic and parameters of the facet and AR layers. SPWG is replaced with a medium with an equivalent refractive index of 3.39.

SPWG facet is relatively, efficient, provided that the discontinuity of dielectric (i.e., nonmetallic) regions to the left and right of facet is small [23]. However, to meet practical device requirements facet (power), reflectivity should typically be kept below 10^{-4}. Along with other methods, antireflection (AR) coating is widely used to reduce facet reflectivity. The standard design method of multilayer AR coatings is based on the optical admittance matching [24] for a plane wave propagating in a structure in which the waveguide is replaced with a homogeneous medium having an equivalent refractive index [25]. Since waveguide modes are not exactly plane waves, a better approach is to decompose a waveguide mode into its constituent plane waves, find the reflected plane waves from the facet, add up all these reflections to find the total reflected field, and finally, calculate the overlap of the reflected field and waveguide mode to obtain the mode reflectivity [28], [29]. Based on this approach, we give an example of the design of a double-layer AR coating for a SLD with the proposed SPWG system. The SPWG is replaced with a dielectric medium with refractive index equal to the symmetric mode effective index. The mode reflectivity is obtained from [12]

$$R = \left| \frac{\int_{-\infty}^{\infty} k_e r(s) H^2(s) ds}{\int_{-\infty}^{\infty} h^2(x) dx} \right|^2. \tag{11}$$

Here, $h(x)$ is the H_y field of the symmetric mode, and $H(s)$ is its Fourier transform given by

$$H(s) = \int_{-\infty}^{\infty} h(x) e^{ik_e sx} dx. \tag{12}$$

$k_e = k_0 n_{eff}$, where n_{eff} is the effective index of the symmetric SP mode, and $r(s)$ is the Fresnel reflection coefficient for a plane wave incident on the AR layers with angle $\theta_0 = \sin^{-1}(s)$ [27]. The inset of Fig. 6 shows the schematic diagram of the SPWG facet with two layers of AR coating designed based on the method outlined in [24]. The reflectivity of the symmetric mode as a function of wavelength is plotted in Fig. 6. It is less than 10^{-4} over a wavelength range of about 135 nm and less than 2×10^{-4} over a wavelength range of about 145 nm centered at $\lambda_0 = 1.55$ μm. This shows the advantage of a two-layer coating system over a single-layer coating. More bandwidth can be achieved with a higher number of AR layers.

6. SPWG-SLD Device Performance

To simulate the SPWG-SLD operation, a 1-D mixed-frequency-time domain method [26] has been used. In this method, the device length (along the z-direction), as well as the spectral range of spontaneous emission, is divided into a number of spatial and spectral slices, respectively. Two

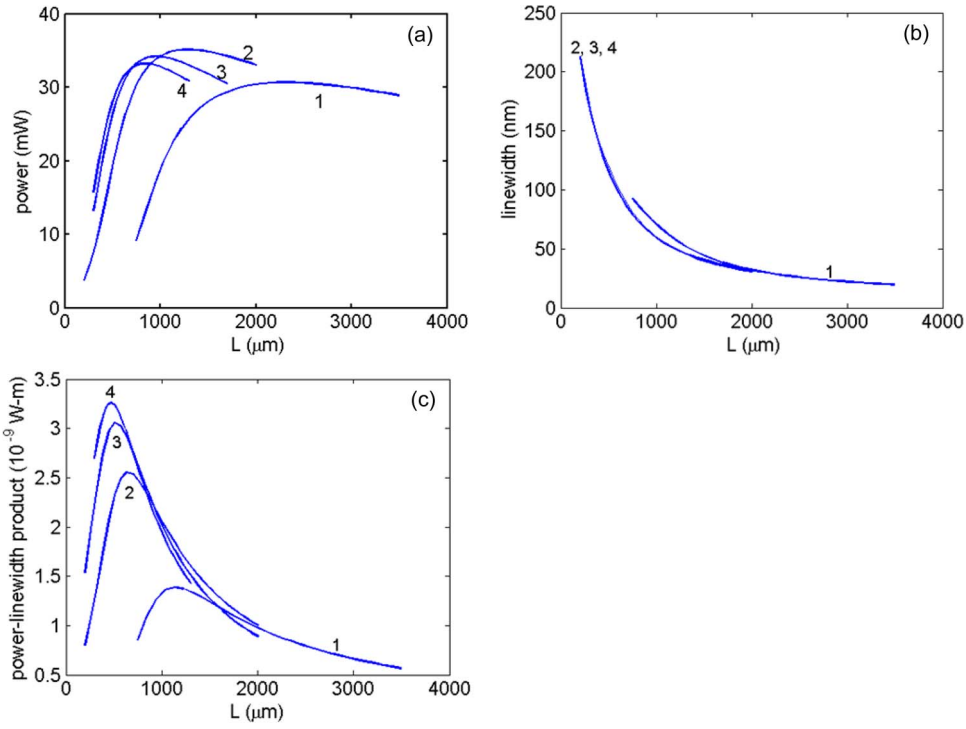

Fig. 7. (a) Output power, (b) linewidth, and (c) power-linewidth product of SLDs with dielectric waveguide and SPWG versus device length. 1,dielectric waveguide SLD; two-, three-, and four-, with five-layer SPWG different only in buffer layer thicknesses of 0, 50, and 100 nm, respectively.

photon rate equations for each spectral slice (one for forward and one for backward propagating waves) and one carrier rate equation for the whole spectrum are derived as

$$\frac{\partial P_{f,r}(z,t,\lambda_k)}{v_g \partial t} \pm \frac{\partial P_{f,r}(z,t,\lambda_k)}{\partial z} = [\Gamma g(z,t,\lambda_k) - \alpha_s] P_{f,r}(z,t,\lambda_k) + P^s_{f,r}(z,t,\lambda_k) \tag{13}$$

$$\frac{\partial N(z,t)}{\partial t} = \frac{I}{qdwL} - \left[A + BN(z,t) + CN^2(z,t)\right] N(z,t) - R_{stim}(z,t) \tag{14}$$

and solved after suitable numerical discretization. In the above equations, $P_{f,r}$ are the forward/backward propagating power waves of the SPWG mode, λ_k is the center wavelength of the kth spectral slice, and $P^s_{f,r}$ are the spontaneous emission power coupled into an individual spectral slice at a certain time and position along the device given by

$$P^s_{f,r}(z,t,\lambda_k) = \beta R_{sp}(z,t,\lambda_k) h\nu_k wd. \tag{15}$$

R_{sp} and R_{stim} are the spontaneous and stimulated recombination rates [30], respectively, w and d are the active region width and thickness, and $h\nu_k$ is the photon energy at the center of the spectral slice k. At the left and right facets $(z = 0, L)$, forward and backward propagating waves are related to reflectivities R_l and R_r by

$$P_f(0,t,\lambda_k) = R_l P_r(0,t,\lambda_k) \tag{16a}$$

$$P_r(L,t,\lambda_k) = R_r P_f(L,t,\lambda_k) \tag{16b}$$

Other parameters in (13) and (14) have their usual definitions as in [26]. The advantage of this model is that it captures effects such as the longitudinal spatial hole burning (LSHB) and the spectral characteristics of the device operation.

Using the above model, we have simulated four single QW SLD devices: one with a conventional dielectric waveguide and three with SPWG proposed in Fig. 1(b), all emitting at 1.55 μm. Fig. 7

compares their output power, FWHM linewidth of the output spectrum, and power-linewidth product versus the device length at a constant injection current of 100 mA. For the device with dielectric waveguide (curves labeled 1 in Fig. 7), a value of $\beta = 1\%$ was used for the spontaneous emission coupling factor [13]. For the SPWG devices (curves labeled 2, 3 and 4 in Fig. 7), β was obtained from (10) for the perpendicular dipole. To obtain maximum possible β for the SPWG devices, it is assumed that the QW active region has a tensile strain such that 75% of the excitons in the active region have perpendicular polarization. Therefore, a factor of 0.75 should be included in (10). The SPWG devices have buffer layers of refractive index 3.5 and thicknesses of 0, 50 and 100 nm for devices labeled 2, 3 and 4, respectively, resulting in $\beta = 12.75\%, 26.25\%,$ and 34.5% for the three devices. The cladding regions have index of 3.35 $(\varepsilon = 11.2)$ as in previous simulations. The confinement factor for all devices is set to 0.01 [15]. A loss coefficient of $\alpha = 5$ cm^{-1} is used for the dielectric waveguide SLD. For the three SPWG SLDs, this value has been added to the loss coefficient of the corresponding SPWG system obtained from Fig. 3, yielding $\alpha = 8.2, 13,$ and 16.3 cm^{-1}, respectively.

From Fig. 7, the output power reaches its maximum at an optimal device length. If the length is further increased, device gain decreases due to the carrier dilution effect in the active region, whereas if the length is decreased from the optimal value, the total device gain given by (3) drops, leading, in both cases, to a decreased output power. Linewidth, on the other hand, decreases monotonically as the device length increases. Despite higher loss coefficient for the SPWG, the output power of devices 2, 3, and 4 are higher than that of device 1. Device 2 has higher power than other SPWG devices because its loss coefficient is smaller. An important observation is that SPWG SLDs achieve their maximum output power at a shorter device length than does the dielectric waveguide SLD. At equal device lengths, the emission linewidth of the device 1 is larger than the linewidth of other three devices. However, because of the mentioned feature of the output power and linewidth curves, the power-linewidth products for the SPWG devices are considerably higher. We compare SLD 4 with SLD 1 in two operating points: maximum power-linewidth product and maximum output power. The maximum power-linewidth product for SLD 4 is 3.3 mW-μm at the device length of 470 μm with the output power of 27.5 mW and linewidth of 120 nm. For SLD 1, the maximum power-linewidth product is 1.39 mW-μm, at the device length of 1130 μm, where the output power is 22.5 mW, and linewidth is 62 nm. SLD 4, therefore, outperforms SLD 1 in both output power and linewidth. Now, consider the two devices at their maximum power point. In this case, SLD 4 has an output power of 33 mW at the device length of 845 μm with a linewidth of 71 nm. For SLD 1, the maximum power is 30 mW at a device length of 2360 μm, and the linewidth is 27 nm. Again, SLD 4 has the advantage of having both higher power and higher linewidth. In both the operating conditions considered, SLD 4 has a smaller length than SLD 1.

7. Summary

The performance of a SLD can be significantly enhanced by using the proposed five-layer SPWG and a QW active region which mostly produces perpendicular dipoles (excitons). There is an optimal dipole-metal film distance at which maximum coupling to the LRSP mode occurs. All three devices shown in Fig. 7 with SPWG have both higher output power and power-linewidth product compared with the device with dielectric waveguide. Nevertheless, SPWG devices can be tailored to either the highest power or highest power-linewidth product. To achieve a higher power, SPWG loss should be minimum. This suggests a SPWG with no buffer layer. On the other hand, an SPWG with thick and high index buffer layers has a higher spontaneous coupling factor, which results in a device with a higher power-linewidth product.

References

[1] W. Barnes, A. Dereux, and T. W. Ebbesen, "Surface plasmon subwavelength optics," *Nature*, vol. 424, no. 6950, pp. 824–830, Aug. 2003.

[2] D. Pacifici, H. J. Lezec, and H. A. Atwater, "All-optical modulation by plasmonic excitation of CdSe quantum dots," *Nat. Photon.*, vol. 1, no. 7, pp. 402–406, Jul. 2007.

[3] I. Abdulhalim, M. Zourob, and A. Lakhtakia, "Surface plasmon resonance for biosensing: A mini-review," *Electromagnetics*, vol. 28, no. 3, pp. 214–242, Apr. 2008.
[4] Y. Fujikawa, T. Sakurai, and R. M. Tromp, "Surface plasmon microscopy using an energy-filtered low energy electron microscope," *Phys. Rev. Lett.*, vol. 100, no. 12, pp. 126 803-1–126 803-4, Mar. 2008.
[5] M. Righini, G. Volpe, C. Girard, D. Petrov, and R. Quidant, "Surface plasmon optical tweezers: Tunable optical manipulation in the femtonewton range," *Phys. Rev. Lett.*, vol. 100, no. 18, pp. 186 804-1–186 804-4, May 2008.
[6] K. Okamoto, I. Niki, A. Shvartser, Y. Narukawa, T. Mukai, and A. Sherer, "Surface-plasmon-enhanced light emitters based on InGaN quantum wells," *Nat. Mater.*, vol. 3, no. 9, pp. 601–605, Sep. 2004.
[7] R. Kohler, A. Tredicucci, F. Beltram, H. E. Beere, E. H. Linfield, A. G. Davies, D. A. Ritchie, R. C. Lotti, and F. Rossi, "Terahertz semiconductor-heterostructure laser," *Nature*, vol. 417, no. 6885, pp. 156–159, May 2002.
[8] M. J. Hamp and D. T. Cassidy, "Critical design parameters for engineering broadly tunable asymmetric multiple-quantum-well lasers," *IEEE J. Quantum Electron.*, vol. 36, no. 8, pp. 978–983, Aug. 2000.
[9] C.-F. Lin and B.-L. Lee, "Extremely broadband AlGaAs/GaAs superluminescent diodes," *Appl. Phys. Lett.*, vol. 71, no. 12, pp. 1598–1600, Sep. 1997.
[10] K. Magari, Y. Hoguchi, K. Okamoto, H. Yasaka, H. Nagai, and O. Mikami, "High frequency 1.3 μm superluminescent diode with absorbing tapered waveguide," *Electron. Lett.*, vol. 26, no. 18, pp. 1445–1446, Aug. 1990.
[11] T. Takayama, O. Imafuji, Y. Kouchi, M. Yuri, A. Yoshikawa, and K. Itoh, "100-mW high-power angled-stripe superluminescent diodes with a new real refractive-index-guided self-aligned structure," *IEEE J. Quantum Electron.*, vol. 32, no. 11, pp. 1981–1987, Nov. 1996.
[12] T. Saitoh, T. Mukai, and O. Mikami, "Theoretical analysis and fabrication of antireflection coatings on laser-diode facets," *J. Lightw. Technol.*, vol. LT-3, no. 2, pp. 288–293, Apr. 1985.
[13] J. Park and X. Li, "Theoretical and numerical analysis of superluminescent diodes," *J. Lightw. Technol.*, vol. 24, no. 6, pp. 2473–2480, Jun. 2006.
[14] J. L. Pleumeekers, M.-A. Dupertuis, T. Hessler, P. E. Selbmann, S. Haacke, and B. Deveaud, "Longitudinal spatial hole burning and associated nonlinear gain in gain-clamped semiconductor optical amplifiers," *IEEE J. Quantum Electron.*, vol. 34, no. 5, pp. 879–886, May 1998.
[15] M. Ranjbaran and X. Li, "Performance-enhanced superluminescent diode with surface plasmon waveguide," *Opt. Express*, vol. 17, no. 26, pp. 23 643–23 654, Dec. 2009.
[16] J. J. Burke, G. I. Stegeman, and T. Tamir, "Surface-polariton-like waves guided by thin, lossy metal film," *Phys. Rev. B, Condens. Matter*, vol. 33, no. 8, pp. 5186–5201, Apr. 1986.
[17] D. Ahn and S. L. Chuang, "A field-effect quantum-well laser with lateral current injection," *J. Appl. Phys.*, vol. 64, no. 1, pp. 440–442, Jul. 1988.
[18] E. D. Palik, *Handbook of Optical Constants of Solids*. New York: Academic, 1985.
[19] J. Chilwell and I. Hodgkinson, "Thin-film field-transfer matrix theory of planar multilayer waveguides and reflection from prism-loaded waveguides," *J. Opt. Soc. Amer. A, Opt. Image Sci.*, vol. 1, no. 7, pp. 742–753, Jul. 1984.
[20] E. Anemogiannis and E. N. Glytsis, "Multilayer waveguides: Efficient numerical analysis of general structures," *J. Lightw. Technol.*, vol. 10, no. 10, pp. 1344–1351, Oct. 1992.
[21] R. R. Chance, A. Prock, and R. Silbey, "Molecular fluorescence and energy transfer near interfaces," *Adv. Chem. Phys.*, vol. 37, pp. 1–65, 1978.
[22] I. Gontijo, M. Boroditsky, E. Yablonovitch, S. Keller, U. K. Mishra, and S. P. DenBaars, "Coupling of InGaN quantum-well photoluminescence to silver surface plasmons," *Phys. Rev. B, Condens. Matter*, vol. 60, no. 16, pp. 11 564–11 567, Oct. 1999.
[23] R. F. Wallis, A. A. Maradudin, and G. L. Stegeman, "Surface polariton reflection and radiation at end facets," *Appl. Phys. Lett.*, vol. 42, no. 9, pp. 764–766, May 1983.
[24] H. A. Macleod, *Thin-Film Optical Filters,* 2nd ed., Bristol, U.K.: Adam Hilger, 1986.
[25] J. Lee, T. Tanaka, S. Uchiyama, M. Tsuchiya, and T. Kamiya, "Broadband double-layer antireflection coatings for semiconductor laser amplifiers," *Jpn. J. Appl. Phys.*, vol. 36, no. 1A/B, pp. 52–54, Jan. 1997.
[26] J. W. Park, X. Li, and W. P. Huang, "Comparative study on mixed frequency-time domain models of semiconductor laser optical amplifiers," *Proc. Inst. Elect. Eng.—Optoelectron.*, vol. 152, no. 3, pp. 151–159, Jun. 2005.
[27] M. Born and E. Wolf, *Principles of Optics,* 4th ed., New York: Pergamon, 1970.
[28] C. Vassallo, "Polarization-independent antireflection coatings for semiconductor optical amplifiers," *Electron. Lett.*, vol. 24, no. 1, pp. 61–62, Jan. 1988.
[29] L. Atternäs and L. Thylen, "Single-layer antireflection coating of semiconductor lasers: Polarization properties and the influence of the laser structure," *J. Lightw. Technol.*, vol. 7, no. 2, pp. 426–430, Feb. 1989.
[30] G. P. Agrawal and N. K. Dutta, *Semiconductor Lasers*. Berlin, Germany: Springer-Verlag, 1993.